

High Energy Cosmic Rays from Fanaroff-Riley Radio Galaxies

B. Eichmann,^{a,1}

^aRuhr Astroparticle and Plasma Physics Center (RAPP Center), Ruhr-Universität Bochum, Institut für Theoretische Physik IV/ Plasma-Astroteilchenphysik, 44780 Bochum, Germany

E-mail: eiche@tp4.rub.de

Abstract. The extended jet structures of radio galaxies (RGs) represent an ideal acceleration site for High Energy Cosmic Rays (HECRs) and a recent model showed that the HECR data can be explained by these sources, if the arrival directions of HECRs at energies $\lesssim 8$ EeV from a certain RG, Cygnus A, are isotropized.

First, this work introduces the inverted simulation setup in order to probe the isotropy assumption. Here, different extragalactic magnetic field models are compared showing that either a magnetic field of primordial origin that yields a high field strength in the large scale structures of the Universe is needed, or a significant contribution by a multitude of isotropically distributed sources.

Secondly, the HECRs contribution by the bulk of RGs of different Fanaroff-Riley (FR) type is determined. Here, the most recent FR-type dependent radio-to-CR correlations $Q_{\text{cr}} \propto L_{\text{radio}}^{\beta_L}$ are used, and the impact of the slope β_L on the HECRs is analyzed in detail. Finally, it is carved out that FR-II RGs provide a promising spectral behavior at the hardening part of the CR flux, between about 3 EeV and 30 EeV, but most likely not enough CR power. At these energies, FR-I RGs can only provide an appropriate flux in the case of a high acceleration efficiency and $\beta_L \gtrsim 0.9$, otherwise these sources rather contribute below 3 EeV. Further, the required acceleration efficiency for a significant HECR contribution is exposed dependent on β_L and the CR spectrum at the acceleration site.

Keywords: ultra high energy cosmic rays, magnetic fields, radio galaxies

¹Corresponding author.

Contents

1	Introduction	1
2	UHECRs from Cygnus A	3
2.1	Inverted simulation setup	3
2.2	Mean HE CR deflection	4
3	FR radio galaxies as HE CR emitters	6
3.1	Continuous Source Function	8
3.2	Constraints on the HE CR contribution	12
4	Conclusions	14
A	Details on the inverted simulation setup	15
	Bibliography	16

1 Introduction

The origin of the High Energy Cosmic Rays (HECRs) is still one of the great enigmas of modern astrophysics. HE CRs are defined as fully ionized nuclei that penetrate Earth’s atmosphere with an energy above a few PeV — the so-called knee in the energy spectrum — including the most energetic ones, the so-called Ultra High Energy Cosmic Rays (UHECRs) that provide energies above a few EeV — the so-called ankle in the energy spectrum. From observatories like the Pierre Auger Observatory (Auger) and the Telescope Array (TA) experiment at the highest energies as well as KASCADE, KASCADE-Grande and a few other detectors at lower energies, there are basically three main observational characteristics, that describe our current knowledge of the HE CRs:

- (1.) The energy spectrum, which changes at about 0.4 EeV — the so-called second knee — to a steeper power-law distribution with a spectral index of about 3.3 and flattens above the ankle at about 3 EeV to a spectral index of 2.6 and a sharp flux suppression above about 30 EeV [1–3].
- (2.) The chemical composition, that shows a decrease of the fraction of heavier elements between about 0.1 EeV and 2 EeV, changing to an increase at energies > 2 EeV [4–7].
- (3.) The arrival directions, that are usually expressed in terms of the multipoles of their spherical harmonics. Between about 0.01 EeV and 8 EeV there are no significant hints of anisotropy [8]. However, at higher energies Auger recently reported a 5σ detection of a dipole with an amplitude of $\approx 6.5\%$, while higher-order multipoles are still consistent with isotropy [9]. Further analysis showed a significant modulation of the first harmonic in right ascension above 8 EeV, as well as an increase of its amplitude above 4 EeV [10].

A likely source candidate of those extremely energetic particles are radio galaxies (RGs) due to their powerful acceleration sites within the jets, as already noted by Hillas in 1984 [11]. In particular the shocks caused by the backflowing material in the lobes of RGs represent an

ideal acceleration site for HECRs [12]. Fanaroff and Riley classified two major types of radio galaxies [13]: FR-I RGs, in which the jets are terminating within the galactic environment on scales of a few kiloparsec, so that the brightness decreases with increasing distance from the central object; and FR-II RGs, where the jets extend on scales of $\gtrsim 100$ kpc deep into extragalactic space causing an increased brightness with distance. This morphology distinction obviously correlates with radio power, so that sources with $L_{178} \lesssim 2 \times 10^{25} \text{ W Hz}^{-1} \text{ sr}^{-1}$ tend to be FR-I galaxies, while sources with $L_{178} \gtrsim 2 \times 10^{25} \text{ W Hz}^{-1} \text{ sr}^{-1}$ usually have a FR-II morphology.¹

In a recent study [14] — hereafter referred to as E+18 — it is shown that all of the observational characteristics of UHECRs can be explained by Centaurus A, a FR-I RG, and Cygnus A, a FR-II RG, if the arrival directions of the light CRs from Cygnus A get isotropized due to significant deflections by the extragalactic magnetic field (EGMF), providing a rms deflection of $\theta_{\text{rms}} \gtrsim 25^\circ (\bar{E}/100 \text{ EeV})^{-1}$ for a mean energy \bar{E} of the propagating CR. Note that a single source cannot provide an isotropic distribution on a finite observer sphere, as the corresponding phase space distribution cannot be homogeneous. But if the CRs from Cygnus A lack their initial directional information, i.e. $\theta_{\text{rms}} \sim 360^\circ$, it is expected according to E+18 that the total CR contribution by Cygnus A and Centaurus A, which are located at almost opposite directions, provides a good agreement with the dipole strength at $E \sim 8 \text{ EeV}$. Thus, the dipole is predominantly caused by Centaurus A, which is accidentally located at about the same direction as the dipole. However, it needs a heavy ejecta in order to provide enough deflections by the Galactic magnetic field² to obtain an accurate fit to the observed dipole amplitude. Such an ejecta is motivated by interactions within the galactic environment, e.g. gaseous shells [16], where the jet typically dissipates in the case of FR-I RGs. In order to avoid a heavy jet scenario another significant contribution above 8 EeV is needed, that only M87 and Fornax A can provide according to the E+18 model. Due to the lack of reliable arrival directions of events from Cygnus A, the authors do not investigate any additional characteristics of the dipole or constrain the contributions by M87 and Fornax A. However, these individual RGs can only explain the UHECR data, if about 37% of the CRs from Cygnus A around 8 EeV are deflected by more than $\sim 300^\circ$, hence, the initial CR momentum needs to be isotropized.

Unfortunately, the magnetic fields in extragalactic space and our Galaxy are poorly known, and one of the most sophisticated descriptions of the EGMF, given by Dolag et al. [17] — hereafter referred as D+05, is constrained to a maximal distance of about 120 Mpc. Therefore, the E+18 model does not include the impact of deflections on the CRs from Cygnus A at a distance of about 255 Mpc [18] and a reliable test of the isotropy assumption is missing so far. Further, it needs to be taken into account, that Hackstein et al. [19] — hereafter referred as H+18 — have expanded the D+05 model by introducing the most recent initial conditions of Sorce et al. [20], and provide a set of different EGMF models within a volume of $(500 \text{ Mpc})^3$. There are two basic types of EGMF scenarios: The primordial models with three different seed field assumptions; and the astrophysical models with three different energy budget assumptions, where the impulsive thermal and magnetic feedback in haloes generates the EGMF. Note, that all of these different models are constrained by the local observational data. Nevertheless, the cumulative filling factors³ of the different EGMF models

¹There are notable exceptions to this radio power distinction, like the very powerful FR-I galaxy Hydra A.

²Here, the GMF model of Jansson & Farrar [15] is adopted.

³The filling factor indicates the fraction of the total volume filled with magnetic fields higher than a certain reference value.

differ significantly: In principle, the primordial H+18 models show the highest cumulative filling factors, followed by the astrophysical H+18 models and the D+05 model. Only at field strengths $\lesssim 10^{-12}$ G the D+05 model provides a higher filling factor than the astrophysical H+18 models.

Another important outcome from E+18 has been the subdominance of the UHECR flux by the non-local RG population, i.e. the mean contribution from RGs beyond 120 Mpc, above the ankle. But, its spectral behavior has indicated that a significant contribution below the ankle is still possible. In addition, the description of the average non-local RG population has not differentiated between FR-I and FR-II types, however, FR type dependent radio luminosity functions [21] and radio luminosity to jet power correlations [22, 23] indicate the need for a more detailed investigation of the average HE CR contribution from RGs.

The paper is organized as follows: In Sect. 2 the simulation setup is introduced that provides an estimate of the mean deflections of HE CRs from Cygnus A in the EGMF model of D+05 as well as the models of H+18, and subsequently the “isotropy assumption” is probed. In Sect. 3 the continuous source function of HE CRs is reinvestigated and the average contributions by the bulk of FR-I and FR-II RGs to the observed HE CR flux is constrained. All simulations are carried out with the publicly available code CRPropa3 [24].

2 UHECRs from Cygnus A

To estimate the EGMF effect on HE CRs from Cygnus A, a magnetic field structure up to at least 255 Mpc is needed as well as an efficient propagation algorithm to obtain sufficient statistics.

2.1 Inverted simulation setup

Due to the lack of reliable large-scale EGMF structures, the inner cube of the D+05 field, with an edge length $l_D \simeq 170$ Mpc, is used and continued reflectively at its boundaries. Hence, also the extended EGMF stays divergence free. In a similar manner also the H+18 models are continued up to necessary extension, as the available models⁴ are limited to a volume of $(250 \text{ Mpc})^3$.

Subsequently, an inverted simulation setup is used, where the source is placed at the center of an observer sphere, whose radius is determined by the distance of Cygnus A as sketched in the left Fig. 1. All CR candidates that cross the spherical surface are collected, but kept in the simulation. So, even the proper arrival directions can be estimated by using the zenith angle, as well as the proper spatial positions of the Earth and the source. For more details on the reconstruction of the proper arrival directions as well as a discussion on the corresponding uncertainties the reader is referred to Appendix A.

In principle, the huge benefit of the inverted simulation setup is the significant gain of statistics — with respect to the regular simulation setup used in E+18, since all ejected particles will reach the observer, if no additional constraints are used that reject particles from the simulation. In the following, the impact of energy losses is not taken into account and a maximal trajectory length of 5000 Mpc is used⁵. However, this simulation method is obviously at the expense of an EGMF structure that is able to represent the proper spatial distribution in the local Universe. But, in the case of large scale propagations as well as the absence of extragalactic lenses close to the Earth, it is expected that the impact of the

⁴<https://crpropa.desy.de/>

⁵The Hubble time constraints the maximal trajectory length to about 4423 Mpc.

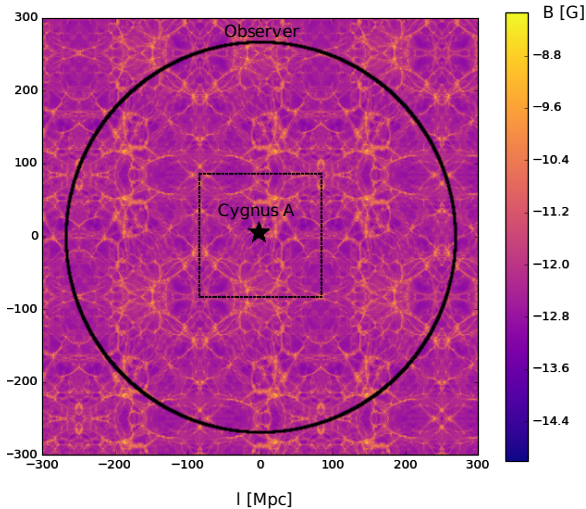


Figure 1: Sketch of the inverted simulation setup with the extended EGMF. The thin dashed line marks the inner cube of the original D+05 field.

EGMF is determined by its large scale properties. Hence, the deflection rather depends on the distance to the source than on its certain spatial position. In the following, 30 arbitrary source positions within the EGMF structure are elaborated in order to avoid the impact of the chosen spatial setting. For each setting, 10^5 individual CR candidates with a fixed rigidity $R \in [50 \text{ PV}, 1000 \text{ EV}]$ are simulated providing a mean deflection $\bar{\theta}$ and a mean trajectory length \bar{l}_{traj} . Note, that the deflection angle θ_i of individual candidates are evaluated using the angle between the detected momentum of the CR candidate and the source-to-point-of-detection vector, so that in the case of large deflections, that cause an isotropization of the final momenta, $\bar{\theta}$ converges towards 90° .

2.2 Mean HECR deflection

If Cygnus A and Centaurus A are the dominant UHECR sources, as suggested by the E+18 model, the arrival directions of CRs from Cygnus A need to be almost isotropically distributed at $E \sim 8 \text{ EeV}$. Thus, the mean deflection needs to be converged towards $\bar{\theta}_{\text{iso}} \sim 90^\circ$.

The left Fig. 2 displays that even at $R \sim 0.1 \text{ EV}$, i.e. a high charge numbers like $Z \sim 26$ for energies above the ankle, the ejected CRs by Cygnus A are not completely isotropized by the EGMF of D+05. In addition, such a heavy CR contribution by Cygnus A can clearly be ruled out, as heavy nuclei suffer from photo-disintegration, so that the CRs can hardly keep such a high charge number while propagating to Earth. Further, an iron dominated ejecta cannot be motivated physically. In the case of a light CR ejecta, i.e. solar like abundances, even source distances of several hundreds of Mpc yield not enough UHECR deflections by the extended D+05 magnetic field to obtain an agreement with the observed dipole amplitudes. Further, the resulting mean trajectory lengths \bar{l}_{traj} almost equals the source distance at rigidities $R \gtrsim 5 \text{ EV}$ as shown by the right Fig. 2.

In contrast, the Fig. 3 shows that the EGMF models by H+18 predict significantly larger deflections and trajectory lengths, in particular for the primordial models due to a significantly higher initial seed field strength compared to D+05. Here, the CR candidates

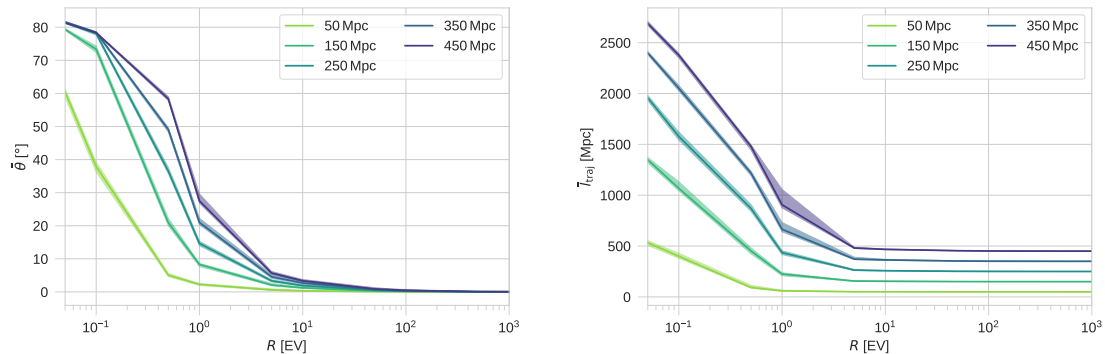


Figure 2: Mean deflections (*left*) and mean trajectory lengths (*right*) of CRs dependent on rigidity in the extended D+05 field for different source distances. The shaded band indicates the uncertainty due to the arbitrary spatial position of the sources.

from Cygnus A can be expected to provide the necessary distribution of arrival directions in order to hold the conclusions from E+18. However, at rigidities below a few hundreds of PV \bar{l}_{traj} exceeds the upper limit that is given by the Hubble time. Thus, the primordial H+18 models also yield that Cygnus A is beyond the magnetic horizon at $R \lesssim 1$ EV. In the case of the astrophysical H+18 models *astrophysicalR* and *astrophysical1R*⁶ the resulting CR deflection are significantly larger than in the case of the D+05 model, but still below $\bar{\theta}_{\text{iso}}$ at ~ 8 EV. The large uncertainties at small rigidities for models with a high cumulative filling factor indicate that the chosen spatial position of the source has a significant impact on the outcome. Hence, the inverted simulation setup only provides accurate results at $R \gtrsim 0.5$ EV for these models.

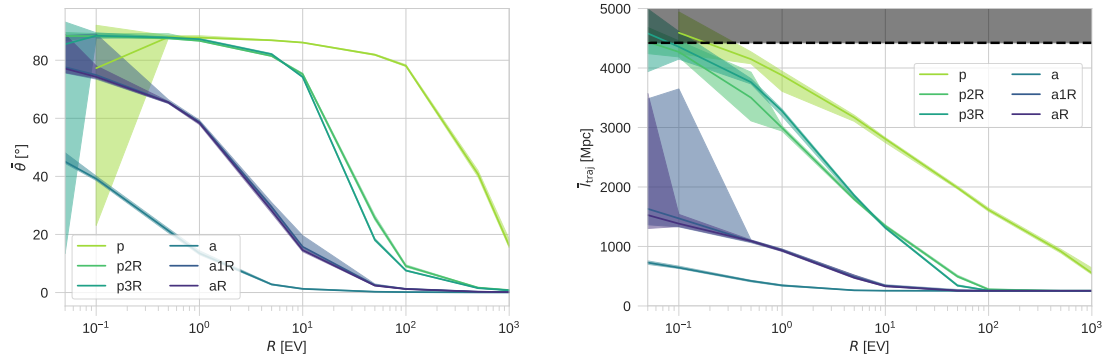


Figure 3: Mean deflections (*left*) and mean trajectory lengths (*right*) of CRs dependent on rigidity in the different H+18 EGMF models — ‘p’ denotes primordial and ‘a’ denotes astrophysical models — for a source at a distance of 250 Mpc. The shaded band indicates the uncertainty due to the arbitrary spatial position of the sources. The dashed black line in the right figure indicates the upper limit of the trajectory length of 4423 Mpc due to the Hubble time.

⁶The *astrophysicalR* model assumes an energy budget per feedback episode of 10^{60} erg from $z = 4$, whereas a changing budget with $(10^{60} \dots 5 \times 10^{58})$ erg for $z = 1 \dots 0$ is supposed in the *astrophysical1R* model.

Summing up, a few single, individual sources, like Cygnus A and Centaurus A, will not be the only dominant HECR sources above the ankle if the EGMF provides a cumulative filling factor of about the astrophysical H+18 model or below — as in the case of the D+05 EGMF. In this case, the dominant contribution up to ~ 8 EeV needs to be provided by a multitude of homogeneously and isotropically distributed sources, as pursued in the following.

3 FR radio galaxies as HECR emitters

The E+18 model already showed that the average non-local source population according to the local radio luminosity function (RLF) from Mauch and Sadler [25] cannot explain the observed spectral behavior above the ankle. But this RLF does not cover the contribution of (rather distant) high-luminous FR-II sources, that dominates the RLF at $L_{151} \gtrsim 10^{26.5} \text{ W Hz}^{-1} \text{ sr}^{-1}$ in the non-local Universe [21]. In addition, the kinetic power of the jet most likely also depends on the FR classification of the source due to different lobe dynamics [23]. In order to constrain the HECR contribution by the bulk of the different types of FR RGs, an appropriate continuous source function (CSF) is needed.

Therefore, the calculations from E+18 are repeated using the RLF from Willott et al. [21] — hereafter referred as W+01 — that differentiates between the FR types and includes the redshift dependence according to the source evolution. In addition, the impact of different ratios of radio luminosity L_{radio} to jet power Q_{jet} , also known as the radiative efficiencies, are investigated. Due to the lack of reliable empirical methods to measure the jet power [23], there are plenty of studies on this issue providing slightly different results. Willott et al. [26] — hereafter referred as W+99 — have derived a popular, model dependent predictor of the jet power of FR-II sources implying a systematic uncertainty $f^{3/2}$ with $1 \leq f \leq 20$. Other analysis have confirmed this $L_{\text{radio}} - Q_{\text{jet}}$ correlation even for FR-I sources [27] within the uncertainty band. However, most of the other predictions yield a rather high f value [28] and a slightly different slope of the correlation [29, 30]. Godfrey and Shabala [22, 23] — hereafter referred as GS13 and GS16, respectively — investigated the hypothesis of a significant difference in the distribution of the energy budget between FR-I and FR-II sources that has not been taken into account so far: In FR-I RGs the energy budget is dominated by a factor of $\gg 100$ by non-radiating particles yielding a rather high f value, while radiating particles dominate this budget in the lobes of FR-II RGs suggesting a low f value. However, the expected difference in the normalization of the $L_{\text{radio}} - Q_{\text{jet}}$ correlation is not observed, and also the theoretically expected difference in the slope β_L of the correlation, due to different jet dynamics, could not be verified so far.

The radio-to-CR correlation provides the energy density in CRs as

$$Q_{\text{cr}} = \frac{g_{\text{m}}}{1+k} Q_{\text{jet}} = \frac{g_{\text{m}}}{1+k} Q_0 \left(\frac{L_{151}}{L_p} \right)^{\beta_L} \quad (3.1)$$

where g_{m} denotes the fraction of jet energy found in leptonic and hadronic matter and the ratio of leptonic to hadronic energy density is given by k . Here, all of the introduced parameters differentiate between FR-I and FR-II. In principle, $g_{\text{m}} < 1$ and in the case of a minimum-energy magnetic field this parameter yields $g_{\text{m}} \simeq 4/7$ [31]. Note, that deviations from the given correlation (3.1) at the order of more than a magnitude occur for individual sources. Based on the most recent models by Godfrey and Shabala the normalization Q_0 is estimated

by equalizing the jet power at the pivot luminosity

$$L_p = \begin{cases} 10^{24}/(4\pi) \text{ W Hz}^{-1} \text{ sr}^{-1} & \text{for FR-I at 151 MHz,} \\ 10^{27.6}/(4\pi) \text{ W Hz}^{-1} \text{ sr}^{-1} & \text{for FR-II at 151 MHz,} \end{cases} \quad (3.2)$$

taken from GS16, to the corresponding jet power given by the GS13 model, which yields

$$Q_0 \simeq \begin{cases} 2.27 \times 10^{43} \text{ erg/s} & \text{for FR-I,} \\ 3.04 \times 10^{45} \text{ erg/s} & \text{for FR-II.} \end{cases} \quad (3.3)$$

Here, a rather large normalization factor ($g = 2$) for the GS13 correlation model of FR-II RGs is supposed. GS16 showed that the empirical methods are strongly affected by the distance dependence, and basically the whole range of $0.5 \lesssim \beta_L \lesssim 1.4$ is possible [23]. Therefore the authors suggest a theoretical approach which leads to a slope of

$$\beta_L = \frac{2}{(3 + \alpha)(1 - n_Q/n_t)} \quad (3.4)$$

if the lobe dynamics are parameterized by $V \propto t^{n_t} Q_{\text{jet}}^{n_Q}$, where V denotes the lobe volume at a given time t . Using a typical radio spectral index⁷ $\alpha \simeq 0.8$, as well as the supersonic, self-similar lobe model [26] for FR-II RGs and the buoyancy lobe model [30, 32] for FR-I RGs, Godfrey and Shabala obtain

$$\beta_L \simeq \begin{cases} 0.5 & \text{for FR-I,} \\ 0.8 & \text{for FR-II.} \end{cases} \quad (3.5)$$

Note, that in the case of powerful FR-I RGs a steeper slope in the range $0.5 \lesssim \beta_L \lesssim 0.8$ is expected.

The Fig. 4 shows that the W+99 model is in good agreement with the FR-II prediction by the GS16 model in the case of low f values. Taking the upper limit of f seriously, the normalization (3.3) cannot exceed 10^{46} erg/s for FR-II. As expected from theory, the predicted jet power of low-luminous FR-I RGs by Godfrey and Shabala is above the W+99 prediction, and the flat slope of the correlation yields a significant increase of the CR contribution by low-luminous FR-I.

In the large scale structures $\gtrsim 1$ pc of radio galaxies the dominant loss time scale is given by the escape time [14] $\tau_{\text{esc}} \simeq r/(\beta_{\text{sh}}c)$ which is estimated by the shock or shear velocity $\beta_{\text{sh}}c$ and the size r of the jet. For the common assumption of Bohm diffusion, which applies at non-relativistic shocks [33, 34], the acceleration takes place on a timescale $\tau_{\text{acc}} = f_{\text{diff}} r_L/(c\beta_{\text{sh}}^2)$ for cosmic-ray particles with a Larmor radius $r_L = R/B$. Here R denotes the particle rigidity, and $1 \lesssim f_{\text{diff}} \lesssim 8$ encapsulates all details of the upstream and downstream plasma properties [35] in a strongly turbulent magnetic field for standard geometries [36]. In steady state, the equality of both time scales yields the maximal rigidity

$$\hat{R} \equiv \frac{E_{\text{max}}}{Ze} = \frac{\beta_{\text{sh}}}{f_{\text{diff}}} B r = g_{\text{acc}} \sqrt{\frac{(1 - g_m) Q_{\text{jet}}}{c}}, \quad (3.6)$$

where the magnetic field power of the jet $Q_B = c\beta_{\text{jet}} \pi r^2 B^2/8\pi = Q_{\text{jet}}(1 - g_m)$ is used. Here, the acceleration efficiency parameter

$$g_{\text{acc}} = \sqrt{\frac{8\beta_{\text{sh}}^2}{f_{\text{diff}}^2 \beta_{\text{jet}}}} \quad (3.7)$$

⁷The flux density S_ν at frequency ν is determined by the radio spectral index according to $S_\nu \propto \nu^{-\alpha}$.

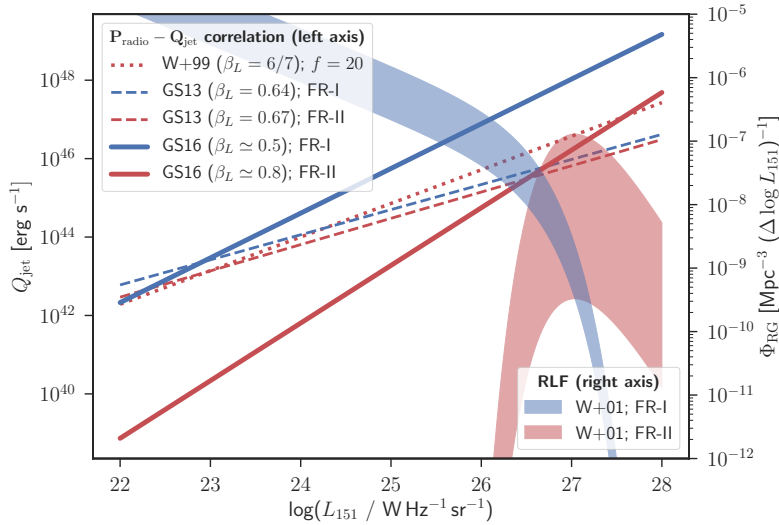


Figure 4: Different models of the radio to jet power correlation (left axis) and the RLF of W+01 derived for model A for an open cosmology ($\Omega_M = 0$) with a redshift $z \in [0, 2]$.

is introduced and in the case of the typical shock and jet velocities $\beta_{\text{sh}} \sim \beta_{\text{jet}} \sim 0.1$ in extended jets of radio galaxies yielding $0.01 \lesssim g_{\text{acc}} \lesssim 1$. Note, that only non-relativistic shocks are considered here, since relativistic ones are poor accelerators to EeV energies [37, 38]. However, mildly relativistic, parallel shocks ($0.2 \lesssim \beta_{\text{sh}} \lesssim 0.5$) are expected to be good UHECR accelerators [38], which still leads to $g_{\text{acc}} \sim 1$ at most. So, the suggested range of g_{acc} also includes the case of a mean free path $\lambda \sim r_L^2/s$, where the magnetic field is randomly orientated on a scale-size $s < r$, or the case of discrete, mildly relativistic shear acceleration [39]. In addition, the shear acceleration scenario provides a hard initial CR spectrum with a spectral index $a \leq 1$, that yields a high energy budget in UHECRs.

Unless otherwise stated, the typical parameter values $g_{\text{acc}} = 0.1$ and $g_m = 4/7$ are used in the following.

3.1 Continuous Source Function

The number of radio sources per volume per power bin yields

$$\frac{dN}{dV dQ_{\text{cr}}} = \frac{\Phi_{\text{RG}}(L_{151}, z)}{2.3 \beta_L Q_{\text{cr}}}, \quad (3.8)$$

where Φ_{RG} denotes the RLF from W+01 of (i) low-luminous radio sources, including FR-I as well as FR-II sources with low-excited/weak emission lines, and (ii) high-luminous radio sources, composed almost exclusively of sources with FR-II radio structures, respectively. In the following, the differentiation of Φ_{RG} based on the FR type is simplified using

$$\frac{dN}{dV dQ_{\text{cr}}} = \begin{cases} \frac{\rho_{\text{lo}}}{2.3 \beta_L Q_{\text{cr}}} \left(\frac{Q_{\text{cr}}}{g_m Q_{\star}} \right)^{-\alpha_{\text{l}}/\beta_L} \exp \left(- \left(\frac{Q_{\text{cr}}}{g_m Q_{\star}} \right)^{1/\beta_L} \right) f_I(z), & \text{for FR-I,} \\ \frac{\rho_{\text{ho}}}{2.3 \beta_L Q_{\text{cr}}} \left(\frac{Q_{\text{cr}}}{g_m Q_{\star}} \right)^{-\alpha_{\text{h}}/\beta_L} \exp \left(- \left(\frac{g_m Q_{\star}}{Q_{\text{cr}}} \right)^{1/\beta_L} \right) f_{II}(z), & \text{for FR-II,} \end{cases} \quad (3.9)$$

Model	Ω_M	$\log(\rho_{l0})$	α_l	$\log(L_{l*})$	z_{l0}	k_l	$\log(\rho_{h0})$	α_h	$\log(L_{h*})$	z_{h0}	z_{h1}	z_{h2}
A	1	-7.153	0.542	26.12	0.720	4.56	-6.169	2.30	27.01	2.25	0.673	-
B	1	-7.150	0.542	26.14	0.646	4.10	-6.260	2.31	26.98	1.81	0.523	-
C	1	-7.120	0.539	26.10	0.706	4.30	-6.196	2.27	26.95	1.91	0.559	1.378
A	0	-7.503	0.584	26.46	0.710	3.60	-6.740	2.42	27.42	2.23	0.642	-
B	0	-7.484	0.581	26.47	0.580	3.11	-6.816	2.40	27.36	1.77	0.483	-
C	0	-7.523	0.586	26.48	0.710	3.48	-6.757	2.42	27.39	2.03	0.568	0.956

Table 1: Best-fit parameters for RLF models A, B and C for $\Omega_M = 1$ and $\Omega_M = 0$, respectively, taken from W+01. Here, ρ_{l0} , ρ_{h0} are in units of $\text{Mpc}^{-3} (\Delta \log(L_{151}))^{-1}$ and L_{l*} , L_{h*} are in units of $\text{W Hz}^{-1} \text{sr}^{-1}$.

where

$$\begin{aligned}
Q_\star &= \begin{cases} \left(\frac{4\pi L_{l*}}{L_p}\right)^{\beta_L} Q_0, & \text{for FR-I,} \\ \left(\frac{4\pi L_{h*}}{L_p}\right)^{\beta_L} Q_0, & \text{for FR-II,} \end{cases} \\
f_I(z) &= \begin{cases} (1+z)^{k_l} & \text{for } z < z_{l0}, \\ (1+z_{l0})^{k_l} & \text{for } z \geq z_{l0}, \end{cases} \\
f_{II}(z) &= \begin{cases} \exp\left(-\frac{1}{2}\left(\frac{z-z_{h0}}{z_{h1}}\right)^2\right) & \text{for model A or models B and C at } z < z_{h0}, \\ 1 & \text{for model B at } z \geq z_{h0}, \\ \exp\left(-\frac{1}{2}\left(\frac{z-z_{h0}}{z_{h2}}\right)^2\right) & \text{for model C at } z \geq z_{h0}, \end{cases}
\end{aligned} \tag{3.10}$$

for two different cosmologies with $\Omega_M = 1$ and $\Omega_M = 0$ for three different parameter models A, B, C. The model dependent best-fit parameters from W+01 are given in Table 1.

Thus, the redshift dependent CSF of FR-I and FR-II sources, respectively, is given by

$$\Psi_i(R, z) \equiv \frac{dN_{\text{cr}}(Z_i)}{dV dR dt} = \int_{\hat{Q}_{\text{cr}}}^{\hat{Q}_{\text{cr}}} S_i(R, \hat{R}(Q_{\text{cr}})) \frac{dN}{dV dQ_{\text{cr}}} dQ_{\text{cr}} \tag{3.11}$$

where $S_i(R, \hat{R}(Q_{\text{cr}})) \equiv dN_{\text{cr}}(Z_i)/dR dt$ denotes the cosmic ray spectrum of element species i with charge number Z_i , emitted by a FR-I/II source with total cosmic ray power per charge number, $Q_{\text{cr},i} \equiv Q_{\text{cr}}(Z_i) = f_i Z_i Q_{\text{cr}}/\bar{Z}$, up to a maximal rigidity $\hat{R}(Q_{\text{cr}})$. The limits of integration are the smallest, \hat{Q}_{cr} , respectively largest, \hat{Q}_{cr} , CR powers that need to be considered.

To solve this integral analytically, one has to suppose that the individual source spectra are given by

$$S_i(R, \hat{R}(Q_{\text{cr}})) = \nu_i(a) Q_{\text{cr}} \left(\frac{R}{\hat{R}}\right)^{-a} \Theta(\hat{R}(Q_{\text{cr}}) - R), \tag{3.12}$$

with the Heaviside step function $\Theta(x)$ that introduces a sharp cutoff at

$$\hat{R}(Q_{\text{cr}}) = g_{\text{acc}} \sqrt{\frac{1}{c} \left(\frac{1}{g_m} - 1\right) (1+k) Q_{\text{cr}}} \tag{3.13}$$

according to Eq. (3.6). Analogous to the approach by E+18, the requirement

$$Q_{\text{cr},i} = \frac{f_i Z_i Q_{\text{cr}}}{\bar{Z}} = e Z_i \int_{\check{R}}^{\hat{R}(Q_{\text{cr}})} dR R S_i(R, \hat{R}(Q_{\text{cr}})), \quad (3.14)$$

yields the spectral normalization correction $\nu_i(a)$ as

$$\nu_i(a) = \frac{f_i}{e \bar{Z} \check{R}^2} \times \begin{cases} (2-a) / (\rho_{\text{cr}}^{2-a} - 1), & \text{for } a \neq 2 \\ 1 / \ln \rho_{\text{cr}}, & \text{for } a = 2 \end{cases} \quad (3.15)$$

with the cosmic ray dynamical range $\rho_{\text{cr}} \equiv \hat{R}(Q_{\text{cr}}) / \check{R}$. For a maximal CR power

$$\hat{Q}_{\text{cr}} > \frac{g_{\text{m}}}{1+k} Q_{\star} \left(\frac{R}{R_{\star}} \right)^2 \quad (3.16)$$

the approximate analytical solution to Eq. (3.11) is given by

$$\Psi_i(R, z) \simeq \begin{cases} \left[\frac{\rho_{\text{lo}} f_i \nu_a c}{2.3 e \bar{Z}} \left[g_{\text{acc}}^2 \left(\frac{1}{g_{\text{m}}} - 1 \right) (1+k) \right]^{-1} \left(\frac{R}{R_{\star}} \right)^{-a} \frac{f_I(z)}{z+1} \right. \\ \quad \left. \times \left[\Gamma \left(\xi_a^I, \left(\frac{R}{R_{\star}} \right)^{2/\beta_L} \right) - \Gamma \left(\xi_a^I, \left(\frac{\hat{Q}_{\text{cr}}(k+1)}{g_{\text{m}} Q_{\star}} \right)^{1/\beta_L} \right) \right] \right], & \text{for FR-I,} \\ \left[\frac{\rho_{\text{ho}} f_i \nu_a c}{2.3 e \bar{Z}} \left[g_{\text{acc}}^2 \left(\frac{1}{g_{\text{m}}} - 1 \right) (1+k) \right]^{-1} \left(\frac{R}{R_{\star}} \right)^{-a} \frac{f_{II}(z)}{z+1} \right. \\ \quad \left. \times \left[\Gamma \left(\xi_a^{II}, \left(\frac{g_{\text{m}} Q_{\star}}{\hat{Q}_{\text{cr}}(k+1)} \right)^{1/\beta_L} \right) - \Gamma \left(\xi_a^{II}, \left(\frac{R_{\star}}{R} \right)^{2/\beta_L} \right) \right] \right], & \text{for FR-II,} \end{cases} \quad (3.17)$$

for the three simplifying cases

$$\begin{aligned} \nu_a = 2 - a; & \quad \xi_a^I = -\alpha_1 + a\beta_L/2; & \quad \xi_a^{II} = \alpha_{\text{h}} - a\beta_L/2; & \quad \text{for } a < 2, a \neq 2 \\ \nu_a = 1 / \ln \rho_{\star}; & \quad \xi_a^I = -\alpha_1 + \beta_L; & \quad \xi_a^{II} = \alpha_{\text{h}} - \beta_L; & \quad \text{for } a \simeq 2 \\ \nu_a = (a-2)\rho_{\star}^{2-a}; & \quad \xi_a^I = -\alpha_1 + \beta_L; & \quad \xi_a^{II} = \alpha_{\text{h}} - \beta_L; & \quad \text{for } a > 2, a \neq 2. \end{aligned}$$

Here, the critical rigidity

$$R_{\star} = g_{\text{acc}} \sqrt{\frac{(1-g_{\text{m}}) Q_{\star}}{c}} = \begin{cases} 8.2 \times 10^{18} g_{\text{acc}} (1-g_{\text{m}})^{\frac{1}{2}} g_1^{\beta_L} \text{ V}, & \text{for FR-I,} \\ 9.5 \times 10^{19} g_{\text{acc}} (1-g_{\text{m}})^{\frac{1}{2}} g_{\text{h}}^{\beta_L} \text{ V}, & \text{for FR-II,} \end{cases} \quad (3.18)$$

is introduced with the RLF model dependent parameters

$$\begin{aligned} g_1 &= \sqrt{\frac{4\pi L_{1\star}}{L_p}} \simeq 39.77 \dots 61.6 \\ g_{\text{h}} &= \sqrt{\frac{4\pi L_{\text{h}\star}}{L_p}} \simeq 1.68 \dots 2.88 \end{aligned} \quad (3.19)$$

as well as the corresponding dynamic range $\rho_{\star} = R_{\star} / \check{R}$.

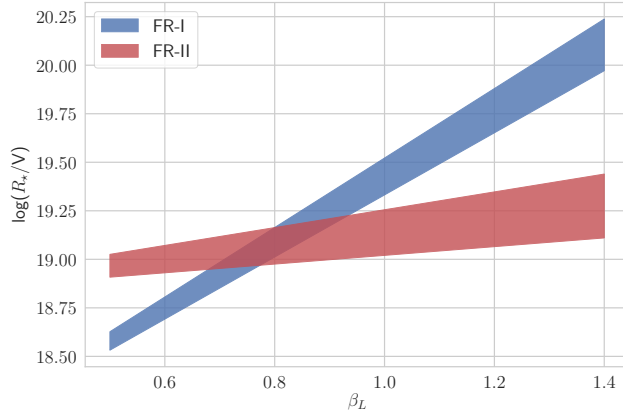


Figure 5: The range of the critical rigidity dependent on β_L for the different RLF models. Here and in the following the typical parameter values of $g_{\text{acc}} = 0.1$, $g_m = 4/7$ are used unless otherwise stated.

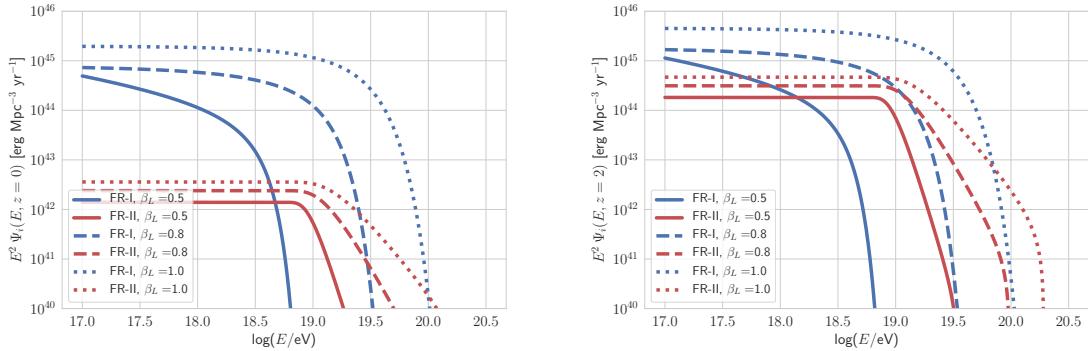


Figure 6: CSF of CR protons from FR-I and FR-II sources with an initial spectral index $a = 2$ and a vanishing leptonic energy fraction $k = 0$ for different β_L in the case of $z = 0$ (left) and $z = 2$ (right).

The Fig. 5 shows that the critical rigidity R_\star of FR-I sources strongly depends on β_L , and in the case of the GS16 model

$$R_\star \sim \begin{cases} 10^{18} \text{ V}, & \text{for FR-I if } \beta_L \simeq 0.5, \\ 10^{19} \text{ V}, & \text{for FR-II if } \beta_L \simeq 0.8 \end{cases} \quad (3.20)$$

for the typical parameter values.

Note, that the critical rigidity is a characteristic of the given distribution of RGs that results from the RLF model, so that it needs to be differentiated from the maximal rigidity of individual sources given by Eq. 3.13. Analyzing the asymptotic spectral behavior of the

CSF (3.17) of FR-I and FR-II sources one recognizes that

$$\begin{aligned} \Psi_i(R \ll R_\star, z) &\propto \left(\frac{R}{R_\star}\right)^{-a}, \\ \Psi_i(R \gg R_\star, z) &\propto \begin{cases} \left(\frac{R}{R_\star}\right)^{-a+2\xi_a^I/\beta_L-2/\beta_L} \exp\left(-\left(\frac{R}{R_\star}\right)^{2/\beta_L}\right) & \text{for FR-I,} \\ \left(\frac{R}{R_\star}\right)^{-a-2\xi_a^{II}/\beta_L} & \text{for FR-II,} \end{cases} \end{aligned} \quad (3.21)$$

so that R_\star denotes a spectral break, where the spectral behavior is no longer governed by the individual sources but gets steepened due to the impact of the RLF. Thus, the spectral behavior of the CSF of FR-I sources is hardly able to explain the observed CR spectrum at $E \gg 1$ EeV for $\beta_L \simeq 0.5$ (see Fig. 6), but these sources provide the necessary UHECR luminosity density of about 10^{44} erg yr $^{-1}$ Mpc $^{-3}$ [40]. These results are in good agreement with the ones from the E+18 model, as well as the luminosity density estimate from Matthews et al. [12]⁸.

In contrast, the spectral behavior of the CSF of FR-II sources is in principle able to explain the data. However, its contribution at small redshifts is significantly smaller than the contribution by FR-Is at about 1 EeV, if similar parameters of g_{acc} , g_{m} and a are supposed — which is not necessarily the case. Nevertheless, the possible parameter range hardly enables FR-II sources to provide the necessary UHECR luminosity density, regardless of their UHECR contribution in the non-local Universe, as the magnetic horizon effect [42] limits the potential contributors to distances of a few hundreds of Mpc. Further details on the resulting HE CR contribution at Earth including the impact of propagation effects are discussed in the following.

3.2 Constraints on the HE CR contribution

Propagation effects need to be included in order to give an accurate estimate of the average contribution of the bulk of FR sources between $z = 0$ and $z = 2$ to the observed HE CR data. Therefore, a 1D simulation is performed, as already introduced by E+18, where the production rate density (3.17) is used to obtain an absolutely normalized CR flux from the bulk of FR sources. In general, a solar-like initial composition is supposed, i.e. 92% H, 7% He, 0.23% C, 0.07% N, 0.5% O, 0.08% Si and 0.03% Fe in terms of number of particles at a given rigidity. The chosen RLF model parameters hardly change the FR-I contribution, however, the FR-II contribution varies almost by an order of magnitude. Unless otherwise stated, the RLF model A for $\Omega_{\text{M}} = 1$ is used in the following, as this setup provides the maximal HE CR contribution.

In the case of the radio-to-CR correlations of GS16 (or GS13) the average HE CR contribution by FR-II sources is even for a high acceleration efficiency and a high cosmic ray load at least a magnitude below the data, as shown in the left Fig. 7, although, its spectral behavior looks quite promising, as already exposed several years ago [43, 44]. Further, it can be shown that even for a hard initial CR spectrum, i.e. $a \ll 2$, the FR-II contribution stays below the data points. Dependent on the critical rigidity R_\star , FR-I sources can provide the HE CR flux below the ankle — especially for $\beta_L \sim 0.5$, as suggested by GS16 — or above for sufficiently large β_L and g_{acc} values. The right Fig. 7 explores the required parameter space of

⁸Note, that the authors used the FR-I based radio-to-CR correlation from Cavagnolo et al. [30] and the local radio luminosity function from Heckman and Best [41]

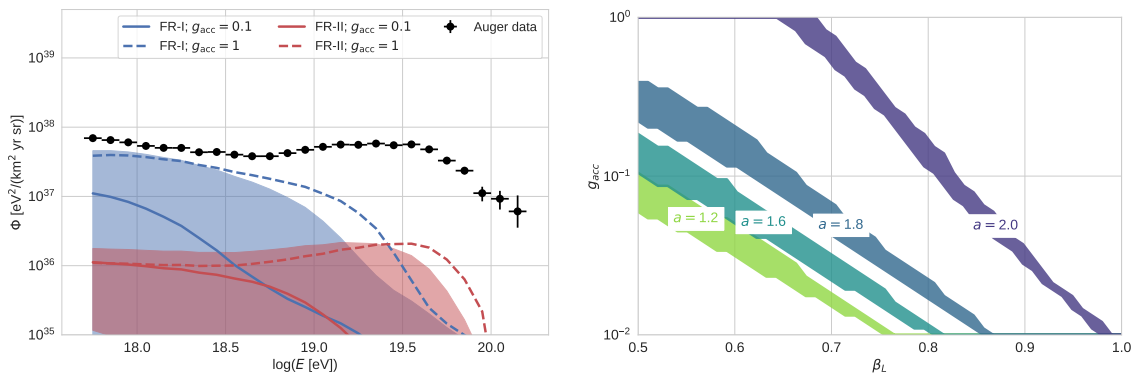


Figure 7: The HECR contribution in the limiting case of $k = 0$ and $g_m = 4/7$:

Left: HECR spectra by FR RGs using $a = 2$ and the radio-to-CR correlation by GS16. The shaded areas indicate the results for $g_{acc} \in [1, 0.01]$ and $g_m \in [0.9, 0.1]$.

Right: The required acceleration efficiency g_{acc} of FR-I RGs dependent on β_L for different spectral indexes a of the initial CR spectrum. The shaded area indicates the uncertainty due to the different parametrization of the RLF of W+01.

FR-I RGs in order to provide a significant contribution of HECRs. So, the typical first order Fermi acceleration spectrum will hardly result in a significant contribution by FR-I RGs, if the leptonic energy budget in the jets is not vanishing, i.e. $k \gtrsim 1$. But in the case of $a \ll 2$, a significant contribution from these sources is expected, even for a small β_L value if $g_{acc} \gtrsim 0.1$.

Based on a simple trial-and-error fitting method, the Fig. 8 introduces two scenarios that provide an accurate CR flux at $10^{18.7} \text{ eV} \lesssim E \lesssim 10^{19.5} \text{ eV}$ by FR-I RGs (scenario I) and FR-II RGs (scenario II), respectively. For the scenario I, a rather high β_L value and a high acceleration efficiency are needed to obtain a critical rigidity (3.18) above $\sim 10^{19.5} \text{ V}$, so that the spectral behavior above the ankle becomes appropriate. For the scenario II, the jet power of FR-II RGs needs to exceed $10^{46} \text{ erg s}^{-1}$ at the pivot luminosity as well as $k \sim 0$, $g_m \sim 4/7$ and $a \lesssim 1.8$ in order to provide enough UHECRs. Due to the impact of the Greisen-Zatsepin-Kuzmin (GZK) effect [45, 46] both scenarios fail at the highest energies. In contrast to scenario I, the scenario II also yields an appropriate HECR flux below the ankle due to the contribution by FR-I RGs. Note, that the necessary contribution from additional sources at higher and lower energies, respectively, most likely changes the given values of the fit parameters.

Further, it has been checked that the resulting cosmogenic neutrino flux is even in the case of the scenario II below the current neutrino limits at energies above 0.1 EeV. Still the associated cosmogenic gamma-ray flux can be in tension with the isotropic diffusive gamma-ray background constraints by Fermi-LAT, due to the strong source evolution behavior of FR-II RGs [47, 48]. However, the spectral index of the initial CR spectrum has about the same influence on the energy density of the diffusive gamma-ray background as the source evolution index [49]. Thus, a rather hard CR spectrum with $a \ll 2$, as also suggested for a discrete, mildly relativistic shear acceleration scenario [39], is favored with the additional benefit of a higher HECR energy budget. However, more detailed fitting scenarios — that include the inevitable contribution of a single (or multiple) individual, close-by source(s), as well as the other observational constraints of HECRs — are needed, but beyond the scope of this work.

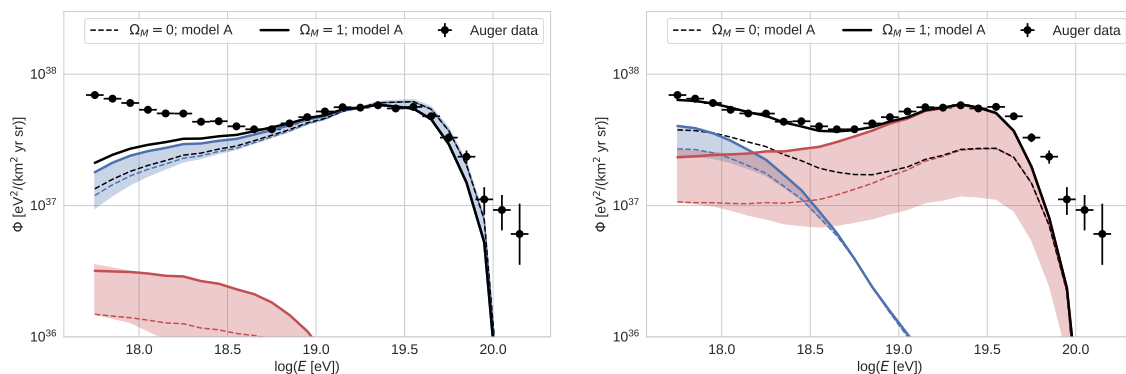


Figure 8: Proof of principle fit scenarios, where the blue/ red lines indicate the individual contributions by FR-I/ FR-II RGs and the shaded bands expose the uncertainty due to the different RLF models:

Left: Scenario I with $a = 1.8$, $g_m = 4/7$ for both FR classes; $\beta_L = 0.9$, $k = 12$, $g_{acc} = 0.8$ for FR-I RGs; and $\beta_L = 0.8$, $k = 0$, $g_{acc} = 0.1$ for FR-II RGs.

Right: Scenario II with $k = 0$, $g_m = 4/7$, $g_{acc} = 0.2$ for both FR classes; $a = 1.88$, $\beta_L = 0.5$ for FR-I RGs; and $a = 1.8$, $\beta_L = 0.8$, as well as a modified normalisation $Q_0 = 2.8 \times 10^{46} \text{ erg s}^{-1}$ for FR-II RGs.

4 Conclusions

In this paper, an extended D+05 EGMF structure and an efficient simulation setup are developed in order to examine the mean deflection $\bar{\theta}$ of CRs from distant sources. In the case of Cygnus A, CRs with a rigidity $\gtrsim 3 \text{ EV}$ yield $\bar{\theta} \lesssim 10^\circ$, so that this source cannot provide the bulk of light CRs at around the ankle, where the observational data features no significant anisotropy so far. This leaves two possible conclusions:

- (i) The EGMF strength needs to be significantly higher than the one given by the D+05 model. Here, the H+18 models are probed as well, showing a substantially different outcome: Due to a significantly higher field strength in the large-scale structures of voids, filaments and sheets, all of the three primordial H+18 models yield UHECR deflections in the necessary order of magnitude for Cygnus A. However, at rigidities $\lesssim 1 \text{ EV}$ the source is already beyond the magnetic horizon.
- (ii) Cygnus A does not contribute significantly to the UHECR data, but a multitude of isotropically distributed sources, most likely radio galaxies or starburst galaxies [50]. Although, the latter source class might struggle to accelerate a nucleus up to the required rigidities [51].

Based on the common radio to jet power correlations, this work determines the average HE CR contribution of the different types of FR RGs dependent on the CR load of the jet, given by g_m and k , the acceleration efficiency g_{acc} , as well as the spectral index β_L of the correlation and the spectral index a of the CRs at the sources. It turns out, that the bulk of FR-II RGs cannot provide enough HE CR power to explain the observed HE CR flux, if $Q_{cr} < 10^{46} \text{ erg s}^{-1}$ at $L_{151} = 10^{26.5} \text{ W Hz}^{-1} \text{ sr}^{-1}$ as suggested by the most recent correlation models. Here, even a vanishing lepton energy budget $k \ll 1$ and a hard initial CR spectrum $a \leq 1$ are not

sufficient. In contrast, there is a large variety of different parameter setups that enable a significant HECR contribution by FR-I RGs. It is shown for a maximal CR load of the jet, i.e. $g_m \sim 4/7$ and $k = 0$, which acceleration efficiency is required dependent on β_L and a .

Finally, two proof of principle scenarios are introduced that enable an explanation of the hardening part of the CR flux at $10^{18.7} \text{ eV} \lesssim E \lesssim 10^{19.5} \text{ eV}$:

- (I) A dominant contribution by FR-I RGs, in the case of a low CR load, but a high acceleration efficiency $g_{\text{acc}} \gtrsim 0.8$ of these sources. However, also a large correlation index $\beta_L \gtrsim 0.9$ is needed, that is disfavored by theoretical expectations of the FR-I lobe dynamics [23].
- (II) A dominant contribution by FR-II RGs, in the case of a significantly higher CR power of these sources with a vanishing lepton fraction. But such an energetically dominant CR population is disfavored by some models [52–54], that suggest $k \gtrsim 1$ in the lobes of FR-II RGs. Nevertheless, such a scenario exhibits some strong implication with respect to the whole HECR data: Supposing that FR-I RGs provide a rather heavy CR contribution with respect to the FR-II class and an individual, close-by FR-I source like Centaurus A provides the observed CRs at energies $\gtrsim 30 \text{ EeV}$ as shown by E+18, even the observed spectral behavior of the chemical composition, as well as the arrival directions are likely explainable. Further, the additional contribution by individual sources can significantly lower the necessary HECR power of FR-II RGs.

However, the northern hemisphere, as covered by the TA experiment, still misses a luminous, close-by FR source that provides the observed CRs above the GZK cut-off energy. Hence, further investigations are needed to give a final answer on the contribution of FR RGs to the HECR data.

Acknowledgments

This work most notably benefits from the development of CRPropa3 and useful discussions with Jörg Rachen. Some of the results in this paper have been derived using the software packages Numpy [55], Pandas [56], Matplotlib [57].

A Details on the inverted simulation setup

In the inverted simulation setup a CR candidate that passes the observer surface needs to stay within the simulation in order to enable the observation of candidates with a deflection angle $\theta_i \geq 90^\circ$. Here θ_i denotes the angle between the normalized arrival direction \vec{a} and the normalized source direction \vec{s} . Thus, even candidates from the far side with respect to the source in a regular simulation setup can be detected. To account for the decreasing detection probability in the case of $\theta_i \rightarrow 90^\circ$, the number of detected candidates has to be corrected by the factor $|\cos \theta_i|^{-1}$.

So, even the proper arrival direction can be determined by $\vec{a}_p = \mathbf{\Omega}_{\text{rot}} \vec{a}$ using the rotation matrix

$$\mathbf{\Omega}_{\text{rot}} = \begin{pmatrix} \cos \omega + \rho_x^2(1 - \cos \omega) & \rho_x \rho_y(1 - \cos \omega) - \rho_z \sin \omega & \rho_x \rho_z(1 - \cos \omega) + \rho_y \sin \omega \\ \rho_x \rho_y(1 - \cos \omega) + \rho_z \sin \omega & \cos \omega + \rho_y^2(1 - \cos \omega) & \rho_y \rho_z(1 - \cos \omega) - \rho_x \sin \omega \\ \rho_x \rho_z(1 - \cos \omega) - \rho_y \sin \omega & \rho_y \rho_z(1 - \cos \omega) + \rho_x \sin \omega & \cos \omega + \rho_z^2(1 - \cos \omega) \end{pmatrix}.$$

Here, the rotation axis

$$\vec{\rho} = \frac{\vec{s} \times \vec{s}_p}{|\vec{s} \times \vec{s}_p|}$$

with the normalized, proper source direction \vec{s}_p , and the rotation angle $\omega = \arccos(\vec{s} \cdot \vec{s}_p)$ need to be determined at first.

The error of the inverted setup is on the one hand side exposed by the error bands in the Figures 2 and 3, which show the standard deviation based on the chosen spatial position of the source. But on the other hand, also a given spatial setting causes an uncertainty based on the spread of the resulting distribution of deflections, as the inverted simulation setup necessarily provides the sum of all possible deflections dependent on the given distance to the source. Thus, the absolute error of a chosen setting is given by $\Delta\theta = \sum_i \|\bar{\theta} - \theta_i\|$, where $\bar{\theta}$ denotes the mean deflection. Using the extended EGMF structure of D+05 for a source at a distance of 250 Mpc, the distribution of θ_i with respect to $\bar{\theta}$ is analyzed as shown in Fig. 9. Thus, the maximal deflection error $\Delta\hat{\theta}$ for a given percentage of CRs dependent on its rigidity is provided as shown in the right Fig. 9. Here, the narrow bands indicate, that the chosen spatial setting hardly change the resulting maximal deflection error. A small percentage of candidates yields $\Delta\hat{\theta}$ of more than 90° at a few hundreds of PV, that converges towards 90° with decreasing rigidity due to the increase of $\bar{\theta}$. But even at these rigidities, the majority of CRs still deviates from $\bar{\theta}$ by less than $\sim 50^\circ$. At 1 EV only about 5% of the CR candidates provide a deflection error of more than about 16° , that continuously decreases to about 5° at 8 EV. Only about 1% of the sky

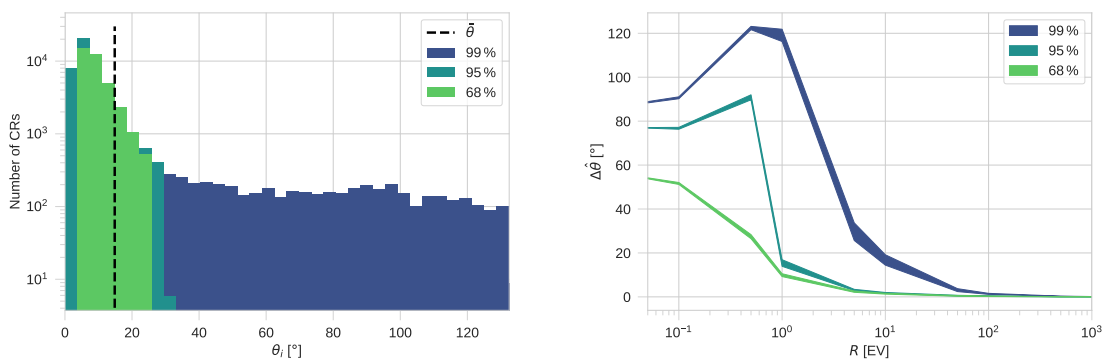


Figure 9: Deflections in the D+05 EGMF for a source at a distance of 250 Mpc.

Left: Different percentages of the distribution of θ_i that are the closest to $\bar{\theta}$ (dashed line) for CRs with a rigidity $R = 1$ EV. *Right:* Maximal absolute deflection error of a given percentage of the individual CR candidates. The bands refer to the scattering that results from the effect of 30 arbitrary source positions.

provides significant deflections errors at the order of several tens of degree at these rigidities, which is in good agreement with the extrapolation results by D+05. Thus, a significant over- or underestimate of the mean deflections of the HECRs with respect to the proper spatial position of Cygnus A in a regular simulation setup is not to be expected.

References

- [1] D. R. Bergman and J. W. Belz, *Cosmic rays: the second knee and beyond*, *Journal of Physics G: Nuclear and Particle Physics* **34** (2007), no. 10 R359.
- [2] **HiRes** Collaboration, R. U. Abbasi et al., *First Observation of the Greisen-Zatsepin-Kuzmin Suppression*, *Phys. Rev. Lett.* **100** (2008) 101101, [[astro-ph/0703099](#)].
- [3] **Pierre Auger** Collaboration, J. Abraham et al., *Measurement of the Energy Spectrum of Cosmic Rays above 10^{18} eV using the Pierre Auger Observatory*, *Phys. Lett. B* **685** (2010) 239–246, [[arXiv:1002.1975](#)].
- [4] **Pierre Auger** Collaboration, J. Abraham et al., *Measurement of the Depth of Maximum of Extensive Air Showers above 10^{18} eV*, *Phys. Rev. Lett.* **104** (2010) 091101, [[arXiv:1002.0699](#)].
- [5] K.-H. Kampert and M. Unger, *Measurements of the cosmic ray composition with air shower experiments*, *Astroparticle Physics* **35** (2012), no. 10 660 – 678.
- [6] **Pierre Auger** Collaboration, A. Aab et al., *Depth of Maximum of Air-Shower Profiles at the Pierre Auger Observatory. II. Composition Implications*, *Phys. Rev.* **D90** (2014) 122006, [[arXiv:1409.5083](#)].
- [7] **Pierre Auger** Collaboration, M. Unger for the Pierre Auger Collaboration, *Highlights from the Pierre Auger Observatory*, *PoS ICRC2017* (2017) 1102, [[arXiv:1710.09478](#)].
- [8] W. D. Apel et al., *Search for Large-scale Anisotropy in the Arrival Direction of Cosmic Rays with KASCADE-Grande*, *The Astrophysical Journal* **870** (2019), no. 2 91.
- [9] **Pierre Auger** Collaboration, A. Aab et al., *Observation of a Large-scale Anisotropy in the Arrival Directions of Cosmic Rays above 8×10^{18} eV*, *Science* **357** (2017), no. 6537 1266–1270, [[arXiv:1709.07321](#)].
- [10] **Pierre Auger** Collaboration, A. Aab et al., *Large-scale cosmic-ray anisotropies above 4 EeV measured by the pierre auger observatory*, *The Astrophysical Journal* **868** (nov, 2018) 4.
- [11] A. M. Hillas, *The Origin of Ultrahigh-Energy Cosmic Rays*, *Ann. Rev. Astron. Astrophys.* **22** (1984) 425–444.
- [12] J. H. Matthews, A. R. Bell, K. M. Blundell, and A. T. Araudo, *Ultrahigh energy cosmic rays from shocks in the lobes of powerful radio galaxies*, *Monthly Notices of the Royal Astronomical Society* **482** (2019), no. 4 4303–4321.
- [13] B. L. Fanaroff and J. M. Riley, *The Morphology of Extragalactic Radio Sources of High and Low Luminosity*, *Mon. Not. Roy. Astron. Soc.* **167** (1974) 31P–36P.
- [14] B. Eichmann, J. Rachen, L. Merten, A. van Vliet, and J. B. Tjus, *Ultra-high-energy cosmic rays from radio galaxies*, *Journal of Cosmology and Astroparticle Physics* **2018** (2018), no. 02 036.
- [15] R. Jansson and G. R. Farrar, *A New Model of the Galactic Magnetic Field*, *Astrophys. J.* **757** (2012) 14, [[arXiv:1204.3662](#)].
- [16] Gopal-Krishna, P. L. Biermann, V. de Souza, and P. J. Wiita, *Ultra-high-energy Cosmic Rays from Centaurus A: Jet Interaction with Gaseous Shells*, *Astrophys. J. Lett.* **720** (2010) L155–L158, [[arXiv:1006.5022](#)].
- [17] K. Dolag, D. Grasso, V. Springel, and I. Tkachev, *Constrained Simulations of the Magnetic Field in the Local Universe and the Propagation of Ultrahigh Energy Cosmic Rays*, *JCAP* **1** (2005) 9, [[astro-ph/0410419](#)].
- [18] S. van Velzen, H. Falcke, P. Schellart, N. Nierstenhöfer, and K.-H. Kampert, *Radio Galaxies of the Local Universe. All-sky Catalog, Luminosity Functions, and Clustering*, *Astron. Astrophys.* **544** (2012) A18, [[arXiv:1206.0031](#)].

- [19] S. Hackstein, F. Vazza, M. Brüggen, J. G. Sorce, and S. Gottlöber, *Simulations of ultra-high energy cosmic rays in the local Universe and the origin of cosmic magnetic fields*, *Monthly Notices of the Royal Astronomical Society* **475** (01, 2018) 2519–2529.
- [20] J. G. Sorce, S. Gottlöber, G. Yepes, Y. Hoffman, H. M. Courtois, M. Steinmetz, R. B. Tully, D. Pomarède, and E. Carlesi, *Cosmicflows Constrained Local Universe Simulations*, *Monthly Notices of the Royal Astronomical Society* **455** (11, 2015) 2078–2090.
- [21] C. J. Willott, S. Rawlings, K. M. Blundell, M. Lacy, and S. A. Eales, *The radio luminosity function from the low-frequency 3CRR, 6CE and 7CRS complete samples*, *Monthly Notices of the Royal Astronomical Society* **322** (2001), no. 3 536–552.
- [22] L. E. H. Godfrey and S. S. Shabala, *AGN Jet Kinetic Power and the Energy Budget of Radio Galaxy Lobes*, *The Astrophysical Journal* **767** (2013), no. 1 12.
- [23] L. E. H. Godfrey and S. S. Shabala, *Mutual distance dependence drives the observed jet-power–radio-luminosity scaling relations in radio galaxies*, *Monthly Notices of the Royal Astronomical Society* **456** (2016), no. 2 1172–1184.
- [24] R. Alves Batista et al., *CRPropa 3 - a Public Astrophysical Simulation Framework for Propagating Extraterrestrial Ultra-High Energy Particles*, *JCAP* **1605** (2016) 038, [[arXiv:1603.07142](https://arxiv.org/abs/1603.07142)].
- [25] T. Mauch and E. M. Sadler, *Radio Sources in the 6dFGS: Local Luminosity Functions at 1.4GHz for Star-forming Galaxies and Radio-loud AGN*, *Mon. Not. Roy. Astron. Soc.* **375** (2007) 931–950, [[astro-ph/0612018](https://arxiv.org/abs/astro-ph/0612018)].
- [26] C. J. Willott, S. Rawlings, K. M. Blundell, and M. Lacy, *The Emission Line-Radio Correlation for Radio Sources Using the 7C Redshift Survey*, *Mon. Not. Roy. Astron. Soc.* **309** (1999) 1017–1033, [[astro-ph/9905388](https://arxiv.org/abs/astro-ph/9905388)].
- [27] X. Cao and S. Rawlings, *No evidence for a different accretion mode for all 3CR FR I radio galaxies*, *Mon. Not. Roy. Astron. Soc.* **349** (2004) 1419–1427, [[astro-ph/0312401](https://arxiv.org/abs/astro-ph/0312401)].
- [28] K. M. Blundell and S. Rawlings, *The Spectra and Energies of Classical Double Radio Lobes*, *Astron. J.* **119** (2000) 1111–1122, [[astro-ph/0001327](https://arxiv.org/abs/astro-ph/0001327)].
- [29] L. Birzan, B. R. McNamara, P. E. J. Nulsen, C. L. Carilli, and M. W. Wise, *Radiative Efficiency and Content of Extragalactic Radio Sources: Toward a Universal Scaling Relation between Jet Power and Radio Power*, *The Astrophysical Journal* **686** (2008), no. 2 859–880.
- [30] K. W. Cavagnolo, B. R. McNamara, P. E. J. Nulsen, C. L. Carilli, C. Jones, and L. Birzan, *A Relationship between AGN Jet Power and Radio Power*, *The Astrophysical Journal* **720** (2010), no. 2 1066–1072.
- [31] A. G. Pacholczyk, *Radio Astrophysics. Nonthermal Processes in Galactic and Extragalactic Sources*. W. H. Freeman & Co Ltd, San Francisco, 1970.
- [32] L. Birzan, D. A. Rafferty, B. R. McNamara, M. W. Wise, and P. E. J. Nulsen, *A Systematic Study of Radio-induced X-Ray Cavities in Clusters, Groups, and Galaxies*, *Astrophys. J.* **607** (June, 2004) 800–809, [[astro-ph/0402348](https://arxiv.org/abs/astro-ph/0402348)].
- [33] M. D. Stage, G. E. Allen, J. C. Houck, and J. E. Davis, *Cosmic-ray diffusion near the Bohm limit in the Cassiopeia A supernova remnant*, *Nature Physics* **2** (Sept., 2006) 614–619, [[astro-ph/0608401](https://arxiv.org/abs/astro-ph/0608401)].
- [34] Y. Uchiyama, F. A. Aharonian, T. Tanaka, T. Takahashi, and Y. Maeda, *Extremely fast acceleration of cosmic rays in a supernova remnant*, *Nature* **449** (Oct., 2007) 576–578.
- [35] A. R. Bell, K. M. Schure, B. Reville, and G. Giacinti, *Cosmic-ray acceleration and escape from supernova remnants*, *Monthly Notices of the Royal Astronomical Society* **431** (2013), no. 1 415–429.

- [36] L. O. Drury, *An Introduction to the Theory of Diffusive Shock Acceleration of Energetic Particles in Tenuous Plasmas*, *Rept. Prog. Phys.* **46** (1983) 973–1027.
- [37] A. R. Bell and B. Reville, *On the maximum energy of shock-accelerated cosmic rays at ultra-relativistic shocks*, *Monthly Notices of the Royal Astronomical Society* **439** (02, 2014) 2050–2059.
- [38] A. R. Bell, A. T. Araudo, J. H. Matthews, and K. M. Blundell, *Cosmic-ray acceleration by relativistic shocks: limits and estimates*, *Monthly Notices of the Royal Astronomical Society* **473** (09, 2017) 2364–2371.
- [39] S. S. Kimura, K. Murase, and B. T. Zhang, *Ultrahigh-energy cosmic-ray nuclei from black hole jets: Recycling galactic cosmic rays through shear acceleration*, *Phys. Rev. D* **97** (Jan, 2018) 023026.
- [40] B. A. Nizamov and M. S. Pshirkov, *Constraints on the AGN flares as sources of ultra-high energy cosmic rays from the Fermi-LAT observations*, *arXiv e-prints* (Apr, 2018) arXiv:1804.01064, [[arXiv:1804.01064](https://arxiv.org/abs/1804.01064)].
- [41] T. M. Heckman and P. N. Best, *The coevolution of galaxies and supermassive black holes: Insights from surveys of the contemporary universe*, *Annual Review of Astronomy and Astrophysics* **52** (2014), no. 1 589–660.
- [42] Globus, N., Allard, D., and Parizot, E., *Propagation of high-energy cosmic rays in extragalactic turbulent magnetic fields: resulting energy spectrum and composition*, *A&A* **479** (2008), no. 1 97–110.
- [43] J. P. Rachen and P. L. Biermann, *Extragalactic Ultrahigh-Energy Cosmic Rays. 1. Contribution from Hot Spots in FR-II Radio Galaxies*, *Astron. Astrophys.* **272** (1993) 161–175, [[astro-ph/9301010](https://arxiv.org/abs/astro-ph/9301010)].
- [44] J. P. Rachen, T. Stanev, and P. L. Biermann, *Extragalactic Ultrahigh-Energy Cosmic Rays. 2. Comparison with Experimental Data*, *Astron. Astrophys.* **273** (1993) 377, [[astro-ph/9302005](https://arxiv.org/abs/astro-ph/9302005)].
- [45] K. Greisen, *End to the Cosmic-Ray Spectrum?*, *Phys. Rev. Lett.* **16** (1966) 748–750.
- [46] G. T. Zatsepin and V. A. Kuz'min, *Upper Limit of the Spectrum of Cosmic Rays*, *JETP Letters* **4** (1966) 78.
- [47] A. van Vliet, R. Alves Batista, and J. Hörandel, *Cosmogenic gamma-rays and neutrinos constrain UHECR source models*, *International Cosmic Ray Conference* **35** (Jan., 2017) 562, [[arXiv:1707.04511](https://arxiv.org/abs/1707.04511)].
- [48] N. Globus, D. Allard, E. Parizot, and T. Piran, *Probing the extragalactic cosmic-ray origin with gamma-ray and neutrino backgrounds*, *The Astrophysical Journal* **839** (apr, 2017) L22.
- [49] M. Ahlers and J. Salvado, *Cosmogenic gamma rays and the composition of cosmic rays*, *Phys. Rev. D* **84** (Oct., 2011) 085019, [[arXiv:1105.5113](https://arxiv.org/abs/1105.5113)].
- [50] **Pierre Auger** Collaboration, A. Aab et al., *An Indication of Anisotropy in Arrival Directions of Ultra-high-energy Cosmic Rays through Comparison to the Flux Pattern of Extragalactic Gamma-Ray Sources*, *The Astrophysical Journal* **853** (2018), no. 2 L29.
- [51] J. H. Matthews, A. R. Bell, K. M. Blundell, and A. T. Araudo, *Fornax A, Centaurus A, and other radio galaxies as sources of ultrahigh energy cosmic rays*, *Monthly Notices of the Royal Astronomical Society: Letters* **479** (2018), no. 1 L76–L80.
- [52] J. H. Croston, D. M. Worrall, M. Birkinshaw, and M. J. Hardcastle, *X-ray emission from the nuclei, lobes and hot-gas environments of two FR II radio galaxies*, *Monthly Notices of the Royal Astronomical Society* **353** (2004), no. 3 879–889.
- [53] J. H. Croston, M. J. Hardcastle, D. E. Harris, E. Belsole, M. Birkinshaw, and D. M. Worrall,

An X-Ray Study of Magnetic Field Strengths and Particle Content in the Lobes of FR II Radio Sources, *The Astrophysical Journal* **626** (2005), no. 2 733–747.

- [54] E. Belsole, D. M. Worrall, J. H. Croston, and M. J. Hardcastle, *High-redshift Fanaroff–Riley type II radio sources: large-scale X-ray environment*, *Monthly Notices of the Royal Astronomical Society* **381** (2007), no. 3 1109–1126.
- [55] S. van der Walt, S. C. Colbert, and G. Varoquaux, *The NumPy Array: a Structure for Efficient Numerical Computation*, [arXiv:1102.1523](https://arxiv.org/abs/1102.1523).
- [56] W. McKinney, *Data Structures for Statistical Computing in Python*, *Proc. of SciPy* (2010) 51 – 56.
- [57] J. D. Hunter, *Matplotlib: A 2D Graphics Environment*, *Comput. Sci. Eng.* **9** (2007), no. 3 90–95.